Influence of recent climatic events on the surface water storage of the Tonle Sap Lake

Frédéric Frappart, Sylvain Biancamaria, C. Normandin, F. Blarel, L. Bourrel,
M. Aumont, P. Azemar, P. L. Vu, Thuy Le Toan, B. Lubac, et al.

Influence of recent climatic events on the surface water storage of the Tonle Sap Lake

Frappart F. (1,2), Biancamaria S. (2), Normandin C. (3), Blarel F. (2), Bourrel L. (1), Aumont M. (2), Azemar P. (2), Vu P-L. (1), T. Le Toan (4), Lubac B. (3), Darrozes J. (1)

(1) Géosciences Environnement Toulouse (GET), UMR 5563, CNRS/IRD/Université de Toulouse, OMP-GRGS, 14 Avenue Edouard Belin, 31400 Toulouse, France

(2) LEGOS, Université de Toulouse, CNES, CNRS, IRD, UPS - 14 avenue Edouard Belin, 31400 Toulouse, France

(3) Environnement et Paléo-Environnement Océaniques et Continentaux (EPOC), UMR 5805, CNRS/Université de Bordeaux, Allée Geoffroy Saint-Hilaire, 33615 Pessac, France

(4) Centre d'Etudes Spatiales de la Biosphère (CESBIO), UMR 5126, CNRS/CNES/IRD/Université de Toulouse, 13 Avenue du Colonel Roche, 31400 Toulouse, France

Abstract:

Lakes and reservoirs have been identified as sentinels of climate change. Tonle Sap is the largest lake in both the Mekong Basin and Southeast Asia and because of the importance of its ecosystem, it is has been described as the "heart of the lower Mekong". Its seasonal cycle depends on the annual flood pulse governed by the flow of the Mekong River. This study provides an impact analysis of recent climatic events from El Niño 1997/1998 to El Niño 2015/2016 on surface storage variations in the Tonle Sap watershed determined by combining remotely sensed observations, multispectral images and radar altimetry from 1993 to 2017. The Lake's surface water volume variations are highly correlated with rainy season rainfall in the whole Mekong River Basin (R=0.84) at interannual time-scale. Extreme droughts and floods can be observed when precipitation deficit and excess is recorded in both the Tonle Sap watershed and the Mekong River Basin during moderate to very strong El Niño/La Niña events (R=-0.70) enhanced by the Pacific Decadal Oscillation (R=-0.68). Indian and Western North Pacific Monsoons were identified as having almost equal influence. Below normal vegetation activity was observed during the first semester of 2016 due to the extreme drought in 2015.

2

1. Introduction

Climate variability and human population growth have led to inland waters being identified as some of the most severely endangered ecosystems (Rosenzweig et al., 2007). Lakes and reservoirs are widely distributed around the world and act as integrators of changes occurring in their watershed, the surrounding landscape and the atmosphere (Schindler, 2009; Williamson et al., 2009a). As their physical, chemical, and biological properties respond rapidly to climate-induced changes, they offer a valuable source of information for assessing and monitoring the effects of climate change (e.g., Magnuson, 2000; Lemoalle et al., 2012). Lakes and reservoirs are commonly seen as sentinels of climate change as their physical, chemical, and biological responses to climate variations integrate the changes occurring in their catchment (Adrian et al., 2009; Schindler, 2009; C. E. Williamson et al., 2009).

Tonle Sap Lake in Cambodia is the largest lake and wetland ecosystem in the Mekong River Basin (MRC, 2005). It is considered as the "heart of the Lower Mekong" due to the exceptional biodiversity of its ecosystem (Campbell et al., 2006) and is also one of the most productive ecosystems in the world (Lamberts, 2006) with its high productivity being linked to the flood pulse of the Mekong River (Kummu et al., 2006). The hydrological cycle in the Mekong River Basin is governed by the monsoon regime, itself being strongly influenced by El Niño Southern Oscillation (ENSO). El Niño events are responsible for a decrease in the rainfall, discharge and annual flood period (Räsänen and Kummu, 2013). Conversely, La Niña increases the rainfall, discharge and annual flood period. The combination of climate-related and anthropogenic (hydropower, irrigation) changes in the Mekong River Basin are expected to cause large modifications to the flood pulse of the Tonle Sap (Kummu and Sarkkula, 2008; Västilä et al., 2010). The frequency and intensity of drought and flood events in the region have increased over the past few decades, impacting irrigated fields (Cruz et al.,

2007; Kamoshita and Ouk, 2015). Dam construction and operations in the Chinese Upper

Mekong Basin are also altering the hydrological regime in the Lower Mekong Basin (Stone,

2010; Lu et al., 2014). Development of new hydropower dams in the Chinese Upper Mekong

Basin combined with possible development of thirty-eight new dams in the Vietnamese

Lower Mekong Basin will have a major impact on the hydrological regime of this region (see

Lu et al., 2014 for the impacts on the Chinese Upper Mekong Basin; Arias et al., 2014 for the

impacts on the Vietnamese Lower Mekong Basin).

Remotely sensed observations offer a unique opportunity to continuously monitor floods in

large watersheds. Previous studies have determined spatio-temporal flooding extent by

applying a threshold approach to land surface reflectances, or spectral indexes from the

MODerate resolution Imaging Sensor (MODIS) radiometer (Sakamoto et al., 2007; Arias et

al., 2012; Siev et al., 2016; Fayne et al., 2017) in the Tonle Sap watershed. Gravity Recovery

and Climate Experiment (GRACE) products have recently been used along with MODIS

images to estimate total water storage and identify flood events in the Tonle Sap watershed

(Tangdamrongsub et al., 2016). Estimates of surface water volume changes in the Tonle Sap

watershed are sparse and have only been for short time-periods (e.g., 1997-2005 in Kummu

and Sarkkula, 2008; and 2003-2005 in Siev et al., 2016).

The purpose of this study is to estimate Tonle Sap lake storage variations over the two last

decades and analyze the link between its annual variations with atmospheric forcing,

especially climatic oscillations. Surface water storage variations of the lake are computed over

the 1993-2017 time span, through a synergistic use of flood extent derived from MODIS land

surface reflectances (see sections 3.1 and 4.1) and altimetry-based water levels (see sections

3.2 and 4.2). During these two decades, three extreme droughts (1998, 2015, and 2016) and

three exceptional floods (2000, 2002, and 2011) occurred in the Tonle Sap watershed. In the

following, relationships with climate variability are discussed through comparisons with

climate indices (sections 3.3 and 5.2). A first impact assessment of the extreme drought of

4

90   2015 on the Tonle Sap ecosystem is also presented.

91

2.   Study area

93   Ninety-five percent of the Tonle Sap Lake drainage area is located in Cambodia, with the

94   remaining five percent in Thailand. It is the largest lake and wetland in the Mekong River

95   Basin and the largest lake in Southeast Asia (MRC, 2005; Campbell et al., 2009). Its whole

96   drainage basin occupies an area of 85,800 km² (i.e., 11% of the whole surface of the Mekong

97   basin, MRC 2003) (Fig. 1). The lake-floodplain system extends from 2,400 km² during the

98   low water period to 16,000 km² at peak flood during wet years (Lim et al., 1999; Kummu and

99   Sarkkula, 2008).

100 The catchment incorporates five different land cover classes, as described by Arias et al.,

101 (2012):

102 • Open water (under water from 9 to 12 months a year and covering an area of 3,027 km²),

103 • Gallery forest (annually flooded for 9 months and covering an area of 197 km²)

104 • Seasonally flooded habitats, composed of shrublands and grasslands (annually flooded from 5

105   to 8 months on average and covering an area of 5,409 km²)

106 • Transitional habitats dominated by abandoned agricultural fields, receding rice/floating rice,

107   and lowland grasslands (annually flooded from 1 to 5 months on average and covering an area

108   of 3,658 km²)

109 • Rainfed habitats mostly composed of wet season rice fields and village crops (flooded less than

110   1 month per year and covering an area of 8,641 km²)

111 Tonle Sap Lake is an important ecosystem of Southeast Asia due to its exceptional

112 biodiversity (Campbell et al., 2006). It has been internationally recognized through three

113 Biosphere Reserve core areas under the United Nations Educational, Scientific and Cultural

114 Organization (UNESCO) Programme on Man and the Biosphere (UNESCO, 2006), as well as

115 one Ramsar site under the Ramsar Convention on wetlands (see www.ramsar.org). The Tonle

5

Sap lake ecosystem also supports important fisheries and aquaculture activities. These industries sustain over one million people (Rainboth, 1996; Sverdrup-Jensen, 2002; Hortle, 2007).

The annual monomodal flood pulse in Tonle Sap Lake is governed by the flow in the Mekong River (Junk et al., 2006; Lamberts, 2006). The Tonle Sap River connects the lake to the Mekong River. In the May to September wet season its flow direction is inversed due to water level increase in the Mekong River (Kummu and Sarkkula, 2008). Annual average inflow and outflow are 79.0 and 78.6 km^3, respectively. 57% of the inflow comes from the Mekong mainstem, either through Tonle Sap River discharge (52%) or by overland flooding (5%) (MRCS/WUP-FIN, 2006).

The contributions of Tonle Sap Lake tributaries and direct rainfall into the lake are estimated at around 30% and 13%, respectively (Kummu et al., 2014). Water receding from the lake mostly flows into the Mekong River (88%) or evaporates (12%) (Kummu et al., 2014).

3. Datasets

3.1. Surface reflectances from MODIS

The MODIS spectroradiometer is part of the payload of the Aqua and Terra satellites (launched in 2002 and 1999, respectively). The MODIS sensor acquires radiances in 36 spectral bands. In this study, the MOD09A1 product (8-day binned level 3, version 6) derived from Terra raw radiance measurements were downloaded from the United States Geological Survey (USGS) Earthexplorer website (http://earthexplorer.usgs.gov). It consists in gridded surface reflectances acquired in 7 bands from 620 nm (Red) to 2155 nm (SWIR2) at a resolution of 500 m and corrected for atmospheric effect. This product is obtained by combining the best surface reflectance data of every pixel acquired during an 8-day period for each wavelength. Each MODIS tile covers an area of 1200 km by 1200 km. In this study, 815 composite images from February 2000 to December 2017 were used.

6

141

142   3.2. Radar altimetry data

143 Our radar altimetry data comes from the acquisitions on their nominal orbit of the following missions:

144 Topex-Poseidon (1992-2002), Jason-1 (2002-2008), Jason-2 (2008-2016), Jason-3 (since 2016), ERS-

145 2 (1995-2003), ENVISAT (2003-2010), and SARAL (2013-2016). Topex/Poseidon and Jason-1 to -3

146 missions are on the same 10-day repeat period orbit, whereas ERS-2, ENVISAT and SARAL succeed

147 each other on the same 35-day repeat-period orbit. Altimetry data comes from Geophysical Data

148 Records (GDR) E for Jason-1; GDR D for Jason-2, Jason-3 and SARAL; and GDR v2.1 for

149 ENVISAT delivered by CNES/ESA/NASA processing centers. The data was homogenized and made

150 available by Centre de Topographie des Océans et de l'Hydrosphère (CTOH – http://ctoh.legos.obs-

151 mip.fr). ERS-2 data was reprocessed by CTOH to ensure continuity with ENVISAT for land studies

152 (Frappart et al., 2016). Topex/Poseidon time series come from Frappart et al., (2006b).

153

154   3.3. Ancillary datasets

155   3.3.1 Water level, flood extent and volume

156 Our estimates were compared with the independent dataset made available by ("Impact of the

157 Mekong River Flow Alteration on the Tonle Sap Flood Pulse," 2008) over 1997-2005 consisting of

158 annual minima and maxima water stages, inundation extent and volume. Water stages are from the

159 Kampong Luong station located on the lakeshore. Kummu and Sarkkula (2008) used a Digital

160 Bathymetric Model (DBM) to established polynomial relationships between stage and extent and stage

161 and volume. The DBM was derived from the following three spatial sources: a hydrographic survey

162 (MRC, 1999) to determine the contours of the lake and Tonle Sap River during the dry season; a

163 survey map (Certeza Surveying, 1964) for delineating the Tonle Sap floodplain; and the Shuttle Radar

164 Topography Mission data ("The Shuttle Radar Topography Mission," 2007) for the surrounding areas

165 to complete the DBM (see ("Water balance analysis for the Tonle Sap Lake-floodplain system,"

166 2014)for more details).

7

167

3.3.2 SRTM Digital Elevation Model (DEM)

The Shuttle Radar Topography Mission (SRTM) DEM was derived from the C and X Synthetic Aperture Radar (SAR) images acquired for interferometry purposes on board the space shuttle Endeavour from 11-22 February 2000 (Farr et al., 2007). In this study, the SRTM 1 Arc-Second (30 m) Global elevation data was used in the Tonle Sap watershed. This dataset is available from USGS at: https://eros.usgs.gov/elevation-products.

3.3.3 TRMM/TMPA rainfall

The rainfall product used in this study is the Tropical Rainfall Measuring Mission (TRMM) Multi-Satellite Precipitation Analysis (TRMM/TMPA) 3B43 v7 product. It is a combination of monthly rainfall satellite data and other data sources at a spatial resolution of $0.25°$. This dataset was derived by combining satellite information from the TRMM Microwave Imager (TMI); the Precipitation Radar (PR) and Visible and Infrared Scanner (VIRS) from the TRMM mission (operating from December 1997 to April 2015); the Special Sensor Microwave Imager (SSMI) and Special Sensor Microwave Imager/Sounder (SSMI/S) on board some satellites of the US Air Force Defense Meteorological Satellite Program (DMSP); the Advanced Microwave Scanning Radiometer – Earth Observing System (AMSR-E, operating from June 2002 to October 2011) on board Aqua satellite; Advanced Microwave Sounding Unit (AMSU) and Microwave Humidity Sounder (MHS) on board various meteorological satellites (from 1998 to now); and rain gauge observations. The TRMM 3B43v7 product merges TRMM 3B42-adjusted infrared precipitation with monthly accumulated precipitation from the Global Precipitation Climatology Center ("The TRMM Multi-Satellite Precipitation Analysis (TMPA)," 2010) and is available on the Goddard Earth Sciences Data and Information Services Center (GES DISC) website at: https://mirador.gsfc.nasa.gov/.

3.3.4 MODIS-based Global Land Cover Climatology

8

193 This climatology is based on the Collection 5.1 MODIS Land Cover Type (MCD12Q1) product at 500

194 m spatial resolution and obtained from analysis of MODIS images acquired between 2001 and 2010.

195 A re-analysis attributing a confidence score for each land cover type at each pixel was performed, as

196 substantial interannual variability in land cover types was found to affect 40% of the pixels. The final

197 land cover classification was obtained by choosing the type with the highest confidence score between

198 2001 and 2010 for each pixel (Broxton et al., 2014). This dataset is available from USGS at:

199 https://landcover.usgs.gov/global_climatology.php.

200

201   3.3.5. Climate indices

202   3.3.5.1 El Niño 3.4 Sea Surface Temperature index

203 El Niño Southern Oscillation (ENSO) oceanic indices are defined using Sea Surface Temperature

204 (SST) anomalies in different regions of the Pacific Ocean. El Niño 3.4 SST index is computed over a

205 region located in the eastern Pacific, between longitude 120° W and 170° W and latitude 5° N and 5°

206 S ("Global analyses of sea surface temperature, sea ice, and night marine air temperature since the late

207 nineteenth century," 2003). It is available on a monthly time step starting from January 1870 at:

208 https://www.esrl.noaa.gov/psd/gcos_wgsp/Timeseries/Nino34/.

209

210   3.3.5.2 Pacific Decadal Oscillation index

211 The Pacific Decadal Oscillation (PDO) index is defined as the principal component of monthly SST

212 variability in the North Pacific, poleward of 20° N ("A Pacific Interdecadal Climate Oscillation with

213 Impacts on Salmon Production," 1997). It is available on a monthly time step starting from January

214 1900 at: https://www.esrl.noaa.gov/psd/gcos_wgsp/Timeseries/PDO/.

215

216   3.3.5.3 Monsoon Indices

217 The Indian Monsoon Index (IMI) and the Western North Pacific Monsoon Index (WNPMI) are

218 defined as the difference of 850 hPa zonal wind over the areas (5°N–15°N, 40°E–80°E) and (20°N–

9

30°N, 70°E–90°E), (5°N–15°N, 100°E–130°E) and (20°N–30°N, 110°E–140°E), respectively, between June and September (Wang and Fan, 1999); ("Interannual Variability of the Asian Summer Monsoon," 2001). It is available on a yearly time step from 1948 to 2015 at: http://apdrc.soest.hawaii.edu/projects/monsoon/seasonal-monidx.html.

4. Methods

The lake and floodplain surface extent (section 4.1) and elevation (section 4.2) are first estimated using MODIS and radar altimetry measurements, respectively. They are then combined to compute the lake storage change (section 4.3). Finally, a rainfall standardized anomaly index is computed (section 4.4) to investigate the link between this storage change and rainfall.

4.1. Surface water extent

The approach developed by (Sakamoto et al., 2007) and simplified by Normandin et al., (2018) to monitor flood extent in the Mekong Basin was applied to the Tonle Sap drainage area (processing steps are presented in Figure S1 in the supplementary material section). It is based on the thresholding of the Enhanced Vegetation Index (EVI), the Land Surface Water Index (LSWI), and the Difference Value between EVI and LSWI (DVEL) to determine the status (non-flooded, mixture, flooded, permanent water body) of any pixel in an 8-day composite MODIS image of surface reflectance. These two spectral indexes were selected as the Short-wave infrared (SWIR) band is very sensitive to soil and vegetation moisture content and because the Near infrared (NIR) band presents low surface reflectance values over water bodies and high values over densely vegetated areas, whereas surface reflectance values in the red band are higher for vegetation than over water bodies. Thus, these two indexes are well suited to discriminate between water and vegetation.

The two indexes used in this approach are defined as follows (Huete, 1997):

$$EVI = 2.5 \times \frac{\rho_{NIR} - \rho_R}{\rho_{NIR} + 6 \times \rho_R - 7.5 \times \rho_B + 1} \tag{1}$$

244    $LSWI = \frac{\rho_{NIR} - \rho_{SWIR}}{\rho_{NIR} + \rho_{SWIR}}$ (2)

245   where ρ_{NIR} is the surface reflectance value in the near infrared (841-875 nm, band 2), ρ_R is the surface

246   reflectance value in the red (621-670 nm, band 1), ρ_B the surface reflectance value in the blue (459-

247   479 nm, band 3), and ρ_{SWIR} the surface reflectance in the short-wave infrared (1628-1652 nm, band 6).

248   Following (Sakamoto et al., 2007), the approach summarized in Figure S1 for Normandin et

249   al., (2018) was applied to the series of MODIS images. First, the pixels identified as cloud-

250   covered were filtered out ($\rho_B \geq 0.2$). Then, a linear interpolation was performed to limit

251   information loss over the study area. The pixels are classified into two major classes: non-

252   flooded (EVI > 0.3 or EVI ≤ 0.3 but EVI − LSWI > 0.05) and water-related pixels (EVI ≤ 0.3

253   and EVI − LSWI ≤ 0.05 or EVI ≤ 0.05 and LSWI ≤ 0). This latter class is divided into 3 sub-

254   classes: mixture pixels when 0.1< EVI ≤ 0.3, flooded pixels EVI ≤ 0.1, and long-term water

255   bodies (e.g., rivers and lakes) when a pixel is determined flooded more than 250 days per

256   year. Spatio-temporal variations of the flood were determined in the Tonle Sap drainage basin

257   from February 2000 to December 2017.

258

259   4.2.   Altimetry-based water levels

260   4.2.1 Post-processing of altimeter data

261   Radar altimetry was initially developed to provide accurate measurements of the sea surface

262   topography and is now commonly used for the monitoring of inland water levels (see (Crétaux et al.,

263   2017)2017 for a recent review). Variations of altimeter height from one cycle to another can be

264   associated with water level changes.

265   In this study, we used the Multi-mission Altimetry Processing Software (MAPS) for processing

266   altimetry data over land and ocean (e.g., (Frappart et al., 2015c); (Frappart et al., 2015a); (Biancamaria

267   et al., 2017); Vu et al., 2018), that allows to build time-series of water levels at a virtual station

268   (intersection between satellite track and water body), after a refined selection of the valid altimeter

269   data. Data processing is composed of four main steps:

11

270   i)   a rough delineation of the cross-section between the altimeter tracks and Tonle Sap using

271   Google Earth (Fig. 1b);

272   ii)   loading of the altimetry over the study area and computation of altimeter heights from raw

273   data contained in the GDR;

274   iii)   a refined selection of the valid altimetry data through visual inspection;

275   iv)   computation of the water level time-series as the median of the selected water levels for each

276   cycle.

277   A detailed description of altimetry data processing using MAPS can be found in (Frappart et al.,

278   2015b). MAPS is available via CTOH. Previous studies have shown that Ice-1-derived altimetry

279   heights are the most suitable for hydrological studies in terms of water level accuracy and data

280   availability (e.g., (Frédéric Frappart et al., 2006); (F. Frappart et al., 2006); (Santos da Silva et al.,

281   2010). They are among the commonly available retracked data in the GDR.

282   Measurement bias between missions and difference in satellite track locations were computed and

283   removed from each time series to obtain a consistent time series over the lake between all missions.

284   The final water elevation time series (in meters wrt EGM08 geoid) is computed with reference to

285   ENVISAT track 107 (the most eastward ENVISAT track on the lake, see Fig. 1b).

286

287   4.2.2 Specific processing of Topex-Poseidon and Jason time series

288   As shown in Figure 1b, Topex-Poseidon and Jason track over Tonle Sap Lake is very close to

289   its outlet. Consequently, and as visually observed on Landsat images, during low flow period the

290   observed area is representative of the Tonle Sap River, which connects the lake to the Mekong River,

291   whereas during high flow period it fully includes the lake extent. Correlation between Jason-2 time

292   series and ENVISAT over the period in common (more than 2 years) still remains high (0.9936), with

293   an RMSE of 0.23 m, after removing the common bias between the two time series. For low water

294   elevations (below 5.5 m), Jason-2 water elevations rise before those of ENVISAT and decrease later.

295   This could be due to hydraulic effects: water elevations vary differently in the lake and outlet river

296   because of bathymetry changes. To account for this observation in a simple way, we arbitrarily

297   considered that difference between the two time series can be corrected applying a time lag to Jason-2

298   time series, depending on the water elevations, to get a better match with ENVISAT time series. After

299   different tests on time lags and water elevation thresholds, the best correlation (0.9986) and lowest

300   RMSE between ENVISAT and Jason-2 (0.11 m) are obtained when Jason-2 water elevations below

301   5.5 m are delayed by 9 days, whereas water elevations above this threshold are delayed by 2 days.

302   More information on this issue is shown in Figures S2 to S4 in the supplementary information

303   section. The Topex-Poseidon, Jason-1 and Jason-3 time series used in this study are from the same

304   track and therefore the same processing has been applied (after removing the bias between these time

305   series and Jason-2 time series).

306

307   4.3.   Surface water volume variations

308   MODIS-based flood extents were combined with altimetry-derived water levels to estimate

309   lake volume variations. Due to the extent of flooding in the watershed, our analysis was

310   limited to the pixels which are i) under water filling SRTM DEM with the water stage of the

311   lake (see the supplementary information, section 2, for method) and ii) connected to the lake

312   using a four-connected neighborhood. As flood extent is derived from a shorter time period

313   than water stage (1993-2017 instead of 2000-2017), a polynomial relationship between water

314   stage (h) and lake surface (S) was fitted to estimate surface water extent during the whole

315   altimetry period using Eq. 3:

316     $S(h) = \sum_{i=1}^{n} a_i h^i$ (3)

317   where a_i is the coefficient of degree i of the polynomial and n the maximum degree of the

318   polynomial. A confidence interval of 95%, a RSME of 74 km² and R² of 0.99 were found

319   using a second degree polynomial with the following values: a_0=6013.0 km², a_1=-1518.0 km

320   and a_2=-176.9. As in Baup et al. (2014) or Crétaux et al. (2015; 2016), the volume variations

321   of the lake (ΔV), between two consecutive time steps ($t-1$ and t) were estimated using the

13

322   assumption of a regular morphology of the lake and a pyramidal shape:

323     $\Delta V = \frac{(h(t) - h(t-1)(S(t) + S(t-1) + \sqrt{S(t)S(t-1)})}{3}$ (4)

324

325   4.4. Standardized Precipitation Anomaly Index

326   The Standardized Precipitation Anomaly Index (SPAI) was defined by (Lamb, 1982) to study

327   interannual rainfall variations:

328     $I_R(t) = \frac{1}{n} \sum_{i=1}^{n} \frac{R(i,t) - \langle R(i,\tau) \rangle_{\tau \in T}}{\sigma(R(i,\tau))_{\tau \in T}}$ (5)

329   where $R(i,t)$ is the annual rainfall at TRMM 3B43v7 gridpoint i for hydrological year t,

330     $\langle R(i,\tau) \rangle_{\tau \in T}$ and $\sigma(R(i,\tau))_{t \in T}$ are the annual average and standard deviation over the

331   reference period T at gridpoint i, respectively, and n is the total number of gridpoints in the

332   study area. The hydrological year is defined between November of year t-1 and October of

333   year t.

334

335   **5.   Results and discussion**

336   5.1.   Validation of surface water extent and storage

337

338   Variations of lake surface extent were estimated between February 2000 and December 2017

339   by applying the threshold approach to MODIS images. The average number of days per year

340   with missing data due to cloud presence were computed for each pixel, as well as the

341   associated standard deviation over the whole study period (see Fig. S5 in supplementary

342   information). The annual lack of data due to cloud presence over Tonle Sap Lake and its

343   floodplains is generally less than 8 days (1 image) and can reach up to 24 days (3 images),

344   with standard deviations less than 16 days (2 images). This lack of data (not occurring on

345   consecutive dates) does not prevent the use of MODIS images for monitoring Tonle Sap

346   seasonal flooding. Maps of annual average duration of inundation extent and associated

14

standard deviation are presented in Figures 2a and 2b, respectively, along with maximum and

minimum inundation extents during the flood peak in 2011 (Figs. 2c) and 2015 (Figs. 2d),

respectively, considering only pixels classified as inundated. Fig. 3 is similar to Fig. 2, but

uses both pixels classified as inundated and the ones classified as mixed pixel. Extensive

inundation is generally in the western part of the lake during time spans shorter than 3

months, but can also occur in the eastern part of the lake and along its north to south flowing

tributary in the eastern part of the basin. Longer inundation, lasting between 4 and 5 months

but of smaller extent, can be observed in the lake's outlet and also in the northeastern part

(Fig. 2a). These inundations are characterized by a large interannual variability with standard

deviations between 40 and 50 days (Fig. 2b). In 2011, important inundations (>100 days)

were observed in all eastern and northwestern parts of the lake (Fig. 2c), whereas almost no

flooding was detected in 2015 (Fig. 2d). In addition, considering the mixed pixels (i.e., the

pixels partly inundated), the patterns are similar to those presented in Fig. 2, but with a larger

extent and longer presence (Fig. 3). Floods lasting up to 6 months were detected in the

western parts of the lake (Figs. 3a and 3c), and are in good agreement with results from

previous studies (Kummu and Sarkkula, 2008; Arias et al., 2012; Kummu et al., 2014). Large

differences were obtained between the flood extent using only the flooded pixels and using

both the flooded and mixed pixels in terms of maximum extent and flood duration inside the

maximum inundation extent defined filling SRTM DEM with altimetry-based water stage

(Fig. S6). Even if SRTM DEM exhibits a high frequency noise (variations of 1 or 2 m from

one pixel to another, see Fig. S7), large-scale elevation variations are well retrieved

considering the minimum elevation in the MODIS pixels (Fig. S8) and do not prevent its use

for determining temporal variations of maximum flood extent. In the following, surface water

extents were obtained by considering both the flooded and mixed pixels which are i) under

water filling SRTM DEM with the water stage of the lake and ii) connected to the lake using a

four-connected neighborhood.

15

373   Figure 4a presents temporal variations of surface water extent in the Tonle Sap drainage

374   basin between February 2000 and December 2017 using MODIS images. They exhibit a well-

375   marked seasonal cycle, with minima occurring in April and May and maxima between

376   September and November. There is a strong interannual variability of the maximum flood

377   extent ranging from 5,114 km² in October 2015 up to 13,736 km² in October 2011. The

378   minimum lake surface varies between 2,320 km² in 2016 and 2,800 km² in 2000 during low

379   stage. Water stage changes accordingly, with an annual amplitude (i.e. difference between the

380   maximum and the minimum over the year) varying from 5.5 m in 2015 to 9 m in 2011 (Fig.

381   4b), resulting in volume variations of Tonle Sap lake that range from 31 km^3 in 2015 to 101

382   km^3 in October 2000 and 2011 (Fig. 4c). Comparisons were made using annual amplitude of

383   the lake water stage, inundated surface in the Tonle Sap basin, and water volume estimated by

384   Kummu and Sarkkula (2008) using a Digital Bathimetric Model (DBM) and in situ water

385   levels, over the common period of availability of the different datasets (i.e., 1997-2005 for

386   water stages and volumes, and 2000-2005 for inundated surfaces). A very good agreement

387   was found (in terms of annual amplitude) between altimetry-based and in situ water levels

388   (R=0.97, RMSE=0.27 m and RRMSE=3.5%), and multi-satellite-derived and Kummu and

389   Sarkkula (2008) water volume variations (R=0.96, RMSE=12 km^3 and RRMSE=19%). A

390   good agreement was also found between MODIS-based and Kummu and Sarkkula (2008)

391   surface water extent (R=0.89, RMSE=982 km² and RRMSE=9.9 %). If the very good

392   agreement between in situ and altimetry-based water levels can confirm observations from

393   Topex/Poseidon in a previous study with a RMSE of 0.23 cm (Frappart et al., 2006b), the

394   small discrepancies observed in surface water extent and volume can be attributed to

395   differences of approach in Kummu and Sarkkula (2008) and our own study. The composite

396   DBM including old measurements of the floodplain's topography is liable to introduce some

397   errors to Kummu and Sarkkula's (2008) approach, whereas the delineation of inundation

398   extent using images at the moderate resolution of 500 m and the SRTM DEM is responsible

16

399   for overestimation of the flooded area due to the presence of mixed pixels. Nevertheless, both

400   approaches present very consistent results and can be used to estimate water balance in the

401   drainage area.

402   Over the study period, interannual variations of surface water volume were computed from

403   monthly lake water volume with the removal of monthly climatological averages. The range

404   is between -35.99 km^3 in 2015 to 35.53 km^3 in 2000 (Fig. 5a). The variations were compared

405   with SPAI (see section 4.4) from TRMM/TMPA 3B43 averaged over the Tonle Sap

406   watershed and over the entire Mekong Basin from 1998-2017 (Fig. 5b). Correlation

407   coefficients between the interannual variations of surface water volume and SPAI (defined

408   during the hydrological year between November of year n-1 and October of year n) are equal

409   to 0.61 (p-value=$5.1.10^{-3}$) and 0.77 (p-value=10^{-4}) for the Tonle Sap watershed and the

410   Mekong Basin, respectively. These results are related to the hydrological regime of the Tonle

411   Sap watershed, whose flood pulse is driven by the flow of the Mekong River. Annual

412   precipitation anomalies can account for the large droughts of 1998, 2010 and 2015 and large

413   floods of 2000, 2001 and 2011 with SPAI lower than -1 and higher than 1, respectively, for

414   both the Tonle Sap watershed and the Mekong Basin, but cannot explain the large flood of

415   2002 and large drought of 2016 according to TRMM/TMPA 3B43 dataset. Similar

416   comparisons were performed during the dry and rainy seasons. Correlation coefficients were

417   found equal to 0.31 (p-value=0.19) and 0.84 (p-value close to 0) during the dry and rainy

418   seasons, respectively, for the Mekong Basin and to 0.45 (p-value=$4.5.10^{-2}$) and 0.58 (p-

419   value=$7.5.10^{-3}$) during the dry and rainy seasons, respectively, for the Tonle Sap watershed.

420   These results confirm that surface water volume of the Tonle Sap watershed is strongly

421   influenced by rainfall during the rainy seasons in the Mekong Basin. During the large flood

422   events of 2000, 2001 and 2011, SPAI during the rainy season of between 1 and 1.5 were

423   obtained in the whole Mekong Basin (Fig. 5c). Larger floods were recorded in 2000 and 2011

424   as they were enhanced by SPAI between 1 and 1.5 in the Tonle Sap watershed. A very low

17

positive SPAI was observed in the Tonle Sap watershed during the wet season of 2001. However, high positive anomalies (~2) were observed in the dry season and contributed to the excess in surface water storage for the same year (see Fig.5d). This was also observed in the year 2000, which was the largest flood between 1995 and 2016. Inverse conclusions can be made for the large droughts of 1998, 2010 and 2015 with SPAI between -1.5 and -2 (Fig. 5c) during the wet season. Lower rainfall during the dry season seems to have a low impact as small anomalies were observed during the lowest drought in 2015 (Fig. 5d). The 2002 flood was higher than that of 2001 in spite of a much lower positive SPAI. This was due to a higher than usual lake level at the beginning of the 2002 hydrological year. Conversely, low rainfall deficit was responsible for low water surface storage in 2016 due to the very low lake level at the end of the 2015 hydrological year. For a comparison, the anomaly of lake water volume was 6.8 km^3 in December 2001 and -21.9 km^3 in December 2015. In addition, daily in-situ data of water levels recorded at the Prek Kdam station in the Tonle Sap River (which joins the Mekong River to Tonle Sap Lake) are displayed on the Mekong River Commission website during both dry and flood seasons since 2013 (ffw.mrcmekong.org/historical_rec.htm). A visual inspection showed very similar water stage amplitude between in situ and altimetry time series. Extreme events were defined by considering deviations larger (lower) than two thirds of the maximum (minimum) estimated over the observation period (i.e., around ±24 km^3). Four positive and three negative extrema can be observed. For positive extrema: between July and November 2000, peaking at 36.36 km^3 in September 2000; 24.22 km^3 in September 2001; in September and October 2002, peaking at 35.37 km^3 in September 2002; and in September and October 2011, peaking at 30.77 km^3 in October 2011. For negative extrema: between September and November 1998, peaking at -31.42 km^3 in October 1998; between September and November 2015, peaking at -36.07 km^3 in October 2015; and -24.22 km^3 in September 2011 (Fig. 6a). In the following, we compare these exceptional droughts and floods to climatic indexes to see if they are related to climate variability.

18

451   5.2.   Surface water storage and climate variability

452   Positive anomalies of surface water volume in the Tonle Sap watershed in September-October

453   correspond to negative values of ENSO3.4 index defined by Rayner (2003) (Fig. 6b). On the

454   contrary, negative anomalies of surface water volume in the watershed correspond to positive

455   values of ENSO 3.4. Larger anomalies occur when ENSO index and the Pacific Decadal

456   Oscillation (PDO) index (as defined by Mantua et al (1997)) exhibit large deviations and are

457   in phase. Large positive (respectively negative) anomalies of the lake volume are obtained for

458   moderate (between 1 and 1.5 °C) to very strong (above 2°C) negative (respectively positive)

459   values of both ENSO (El Niño, respectively La Niña, Fig. 6b) and PDO (Fig. 6c) during the

460   previous winter. This phenomenon is caused by a significant intensification of the negative

461   relationship between ENSO and the monsoon when ENSO and PDO are in phase. It was

462   previously described regarding the East Asian monsoon (Kim et al., 2014). Positive values of

463   ENSO and PDO are associated with anomalous warm temperature patterns over East Asia that

464   cause rainfall deficit the following summer. Negative values of ENSO and PDO are linked

465   with anomalous cold temperature patterns, leading to excess rainfall the following summer.

466   On the contrary, when ENSO and PDO are out of phase, interannual variations are lower. The

467   super strong ENSO event in 2015/2016 was an exception, as it did not result in huge rainfall

468   in either the Tonle Sap watershed or the Mekong Basin. This was most likely due to its rapid

469   decay in boreal spring 2016 causing a weakening of the western Pacific subtropical

470   anticyclone (Liu et al., 2017). Correlation between annual amplitude of volume variations and

471   climatic indices were also estimated, and several time-periods were tested. Stronger

472   correlations were found when the ENSO index was averaged over December to February

473   (DJF) as in Räsänen and Kummu (2013) and when the PDO index was averaged over

474   November to March (NDJFM) as in Newman et al., (2003). For $ENSO_{DJF}$, R=-0.70 with a p-

475   value equal to 10^{-4}, whereas for PDO_{NDJFM}, R=-0.68 with a p-value equal to 2.10^{-4}. This

476   confirms earlier findings about relationships in the Mekong Basin between rainfall, discharge,

477 ENSO (Räsänen and Kummu, 2013) and PDO (Delgado et al., 2012). An even higher

478 correlation was found between annual anomalies of surface water storage and ENSO 3.4

479 index than between annual flow and ENSO 3.4 (Räsänen and Kummu, 2013) and this study

480 provides a quantification of the relationship between flood pulse and PDO in the Mekong

481 Basin. The optimal least-squares linear combination of both indices provides a correlation of -

482 0.75. The coefficients of this linear combination are equal to 1.0 and 0.84 for ENSO 3.4 and

483 PDO, respectively. Time series of annual amplitude of lake volume (Fig. 7a), of the ENSO

484 3.4 index averaged over DJF (Fig. 7b) and of the PDO index averaged over NDJFM (Fig. 7c)

485 illustrate differences in the impact of extreme events on lake volume. The drought of 1998

486 and the floods of 2000 and 2011 are directly related to large positive and negative anomalies

487 of both ENSO 3.4 and PDO. The 2002 flood and 2015/2016 droughts can be attributed to both

488 a large value in module of either ENSO 3.4 or PDO (and a lower value of the other index),

489 and the existence of an excess (since 2000) or a deficit (since 2014) of water in the lake. This

490 shows that the possibility of occurrence of a hydrological extreme is not only conditioned by

491 climate factors but also by base water storage from previous years.

492 We propose to quantify the monsoonal impact on lake storage, as the flood pulse in the

493 Mekong Basin is driven by the monsoon. The Mekong Basin is under the influence of both

494 the Indian and the Western North Pacific Monsoons (Delgado et al., 2012). Correlation

495 between anomalies of annual surface water storage and Western North Pacific Monsoons

496 (WNPMI, Wang et al., 2001) and Indian Monsoon (IMI, Wang and Fan 1999) provides better

497 results (R=0.55, p-value=0.006, and R=0.49, p-value=0.018) for July and August,

498 respectively. This is similar to the relationship between water discharge and WNPMI in the

499 downstream Mekong Basin discovered by Delgado et al., (2012).

500

501 5.3) Impact of the 2015 extreme drought on vegetation activity

502 Vegetation activity is highly related to flood duration (Arias et al., 2013). In the following,

20

503 impact of the 2015 drought on the Tonle Sap ecosystem is analyzed using MODIS-derived

504 EVI time series and a land cover map. The 1998 and 2015 extreme droughts were the worst

505 observed during the study period, but MODIS images are onlyavailable since February 2000.

506 Due to this, our analysis is limited to the 2015 drought. Figure 8a shows land cover types

507 from the 500 m MODIS-based Global Land Cover Climatology (Broxton et al., 2014) for the

508 Tonle Sap Basin. Time series of Enhanced Vegetation Index (EVI) and their interannual

509 variations (estimated by removing the climatological monthly mean to the monthly values)

510 were computed for each land cover type. In the following, only land cover types

511 corresponding to vegetation are considered. They are presented for the three main land cover

512 types which cover 80.3% o of the Tonle Sap basin surface (Evergreen Broadleaf Forest,

513 Woody Savannas and Cropland/Natural Vegetation Mosaic) as seen in Figures 8b and c for

514 the time series and associated anomalies, respectively, and in Figures S9a and b for the five

515 other classes of vegetation which cover 14.6% of the surface of the Tonle Sap Basin surface

516 (Mixed Forests, Savannas, Grasslands, Permanent Wetlands and Croplands). Lower than

517 usual minimum values of EVI are observed in spring 2016 for all land cover types as shown

518 in Figures 8b and S9a. The anomalies reached their lowest values in April 2016 for Evergreen

519 Broadleaf Forest, Woody Savannas and Cropland/Natural Vegetation Mosaic with EVI

520 anomalies of -0.11, -0.13 and -0.06 (Fig. 8c), corresponding to an annual variation of

521 amplitude around 0.10, 0.25 and 0.15, respectively. The same timing is observed for

522 Savannas, Grasslands and Permanent Wetland with EVI anomalies of -0.10, -0.05 and -0.12

523 (Fig. S9b), corresponding to an annual variation of amplitude around 0.25, 0.10 and 0.30,

524 respectively. They reached their lowest values in May 2016 for Mixed Forests and Croplands

525 with EVI anomalies of -0.15 and -0.04 (Fig. S9b), corresponding to annual variation of

526 amplitude around 0.10 and 0.15, respectively. The spatial distribution of anomalies of EVI for

527 April and May are presented in Figures 9a and 9b, respectively. They are quite similar to

528 lowest anomaly values in April 2016. The largest negative anomalies are located on the

21

529   Woody Savannas in the northeast and southwest of the watershed, as well as on the Evergreen

530   Broadleaf Forest located in the east and southwest, and the grasslands of the downstream part.

531   Croplands were generally less affected thanks to irrigation. Some rare positive anomalies

532   were also found around the lake. For instance, the extreme drought of 2015 modified

533   vegetation activity during the first semester of 2016. The temporal evolution of EVI of the

534   Evergreen Broadleaf Forest, Woody Savannas and Cropland/Natural Vegetation Mosaic (Fig.

535   10) as well as Savannas, Grasslands and Croplands (Fig. S10) exhibit a longer and lower than

536   usual period of low activity (until June instead of April) where it presents minimum activity

537   between January and June instead of a maximum for Mixed Forests and Wetlands (Fig. S10).

538   Normal and even slightly above normal EVI values are found for the rest of 2016 and also for

539   2017 (Figs. 8b, 8c, S9a and S9b).

540

541   **6.   Conclusion**

542   Surface water storage variations of Tonle Sap were determined combining remotely sensed

543   inundation extent data derived from MODIS reflectance images and altimetry-based water

544   levels from 1993-2017. Their interannual anomalies were found to be more related to the

545   rainfall occurring in the Mekong Basin (R=0.77 for the interannual variations during the

546   whole hydrological year) than in the Tonle Sap watershed (R=0.61) as flooding in the Tonle

547   Sap watershed is mostly driven by the flow of Mekong River. Nevertheless, extreme events

548   (exceptional floods and droughts) occurred when large excess/deficit rainfall occurred during

549   the rainy season in both the Mekong Basin (R=0.84) and Tonle Sap watershed (R=0.58).

550   Excess rainfall occurring in both dry and rainy seasons in the Mekong Basin combined with a

551   rainfall deficit in the Tonle Sap watershed during the rainy season was only seen to cause

552   large flooding in 2001. Important memory effects were also detected as in the extreme flood

553   of 2002. This was mostly due to excess in surface water storage of the exceptional flood of

554   2000 and the large flood in 2001, whereas the extreme drought of 2016 was caused by the

22

deficit in surface water by the drought of 2014 and the extreme drought of 2015. A quasi-equal influence of the West North Pacific and Indian Monsoons was also found with correlations between the interannual variations of surface water storage and the WNPMI in July of 0.55 and the IMI in August of 0.49.

Interannual variations of surface water storage in the Tonle Sap watershed are strongly influenced by climate variability. They exhibit large positive and negative anomalies corresponding to extreme drought (1998, 2015, and 2016) and flood (2000, 2001, 2002, and 2011) events. They were related to the very strong El Niño events of 1997-1998 and 2015-2016 and the moderate La Niña events of 1999-2000 and 2010-2011 enhanced by the PDO. Correlation coefficients between the interannual variations of surface water storage of the Tonle Sap watershed and the average ENSO 3.4 index over DJF and PDO over NDJFM were found equal to -0.70 and -0.68, respectively. R of -0.75 was found using a linear combination of the two former indices. Below normal EVI values for the types of vegetation were observed in the first semester of 2016 as a consequence of the 2015 drought.

The NASA/CNES Surface Water and Ocean Topography (SWOT) mission is to be launched in 2021 and will improve flood monitoring in Tonle Sap by providing water level maps through SAR interferometry techniques at better spatial and temporal resolutions with low impact of cloud presence and vegetation. The data will provide a better understanding of the strong relationship between climatic indices and Tonle Sap lake volume extreme changes, suggested by Räsänen and Kummu (2013) for the whole Mekong basin and therefore help in forecasting the risk of extreme droughts or floods.

23

589

8.   References

591 Adrian, R., O'Reilly, C.M., Zagarese, H., Baines, S.B., Hessen, D.O., Keller, W.,
592   Livingstone, D.M., Sommaruga, R., Straile, D., Van Donk, E., Weyhenmeyer, G.A.,
593   Winder, M., 2009. Lakes as sentinels of climate change. Limnol. Oceanogr. 54, 2283–
594   2297. doi:10.4319/lo.2009.54.6_part_2.2283
595 Arias, M.E., Cochrane, T.A., Kummu, M., Lauri, H., Holtgrieve, G.W., Koponen, J., Piman,
596   T., 2014. Impacts of hydropower and climate change on drivers of ecological productivity
597   of Southeast Asia's most important wetland. Ecol. Model. 272, 252–263.
598   doi:10.1016/j.ecolmodel.2013.10.015
599 Arias, M. E., Cochrane, T. A., Norton, D., Killeen, T. J., Khon, P., 2013. The flood pulse as
600   the underlying driver of vegetation in the largest wetland and fishery of the Mekong Basin.
601   Ambio, 42(7), 864-876, doi: 10.1007/s13280-013-0424-4Arias, M.E., Cochrane, T.A.,
602   Piman, T., Kummu, M., Caruso, B.S., Killeen, T.J., 2012. Quantifying changes in flooding
603   and habitats in the Tonle Sap Lake (Cambodia) caused by water infrastructure
604   development and climate change in the Mekong Basin. J. Environ. Manage. 112, 53–66.
605   doi:10.1016/j.jenvman.2012.07.003
606 Baup, F., Frappart, F., Maubant, J., 2014. Combining high-resolution satellite images and
607   altimetry to estimate the volume of small lakes. Hydrol. Earth Syst. Sci. 18, 2007–2020.
608   doi:10.5194/hess-18-2007-2014
609 Biancamaria, S., Frappart, F., Leleu, A.-S., Marieu, V., Blumstein, D., Desjonquères, J.-D.,
610   Boy, F., Sottolichio, A., Valle-Levinson, A., 2017. Satellite radar altimetry water
611   elevations performance over a 200 m wide river: Evaluation over the Garonne River. Adv.
612   Space Res. 59, 128–146. doi:10.1016/j.asr.2016.10.008
613 Broxton, P.D., Zeng, X., Sulla-Menashe, D., Troch, P.A., 2014. A Global Land Cover Climatology
614   Using MODIS Data. J. Appl. Meteor. Climatol. 53, 1593-1605. doi:10.1175/JAMC-D-13-0270.1
615 Campbell, I.C., Poole, C., Giesen, W., Valbo-Jorgensen, J., 2006. Species diversity and
616   ecology of Tonle Sap Great Lake, Cambodia. Aquat. Sci. 68, 355–373.
617   doi:10.1007/s00027-006-0855-0
618 Campbell, I.C., Say, S., Beardall, J., 2009. Chapter 10 - Tonle Sap Lake, the Heart of the

24

Lower Mekong, in: The Mekong. Academic Press, San Diego, pp. 251–272.

Certeza Surveying. 1964. Final Report to the Committee for Coordination of Investigations of the Lower Mekong Basin. Certeza, Quezon City, The Philippines.

Crétaux, J.-F., Abarca-del-Río, R., Bergé-Nguyen, M., Arsen, A., Drolon, V., Clos, G., Maisongrande, P., 2016. Lake Volume Monitoring from Space. Surv. Geophys. 37, 269–305. doi:10.1007/s10712-016-9362-6

Crétaux, J.-F., Nielsen, K., Frappart, F., Papa, F., Calmant, S., Benveniste, J., 2017. Hydrological applications of satellite altimetry: rivers, lakes, man-made reservoirs, inundated areas., in: Stammer, D., Cazenave, A. (Eds.), Satellite Altimetry Over Oceans and Land Surfaces, Earth Observation of Global Changes. CRC Press.

Crétaux, J.-F., Biancamaria, S., Arsen, A., Bergé-Nguyen, M., Becker, M., 2015. Global surveys of reservoirs and lakes from satellites and regional application to the Syrdarya river basin. Environ. Res. Lett. 10, 015002. doi:10.1088/1748-9326/10/1/015002

Cruz, R.V., Harasawa, H., Lal, M., Wu, S., Anokhin, Y., Punsalmaa, B., Honda, Y., Jafari, M., Li, C., Huu Ninh, N., 2007. Asia. Climate Change 2007: Impacts, Adaptation and Vulnerability. Contribution of Working Group II to the Fourth Assessment Report of the Intergovernmental Panel on Climate Change, Parry, M.L., Canziani, O.F., Palutikof, J.P., van der Linden, P.J., Hanson, C.E. Eds., Cambridge University Press, Cambridge, UK, 469-506

Delgado, J.M., Merz, B., Apel, H., 2012. A climate-flood link for the lower Mekong River. Hydrol. Earth Syst. Sci. 16, 1533–1541. doi:10.5194/hess-16-1533-2012

Farr, T.G., Rosen, P.A., Caro, E., Crippen, R., Duren, R., Hensley, S., Kobrick, M., Paller, M., Rodriguez, E., Roth, L., Seal, D., Shaffer, S., Shimada, J., Umland, J., Werner, M., Oskin, M., Burbank, D., Alsdorf, D., 2007. The Shuttle Radar Topography Mission. Rev. Geophys. 45. doi:10.1029/2005RG000183

Fayne, J.V., Bolten, J.D., Doyle, C.S., Fuhrmann, S., Rice, M.T., Houser, P.R., Lakshmi, V., 2017. Flood mapping in the lower Mekong River Basin using daily MODIS observations. Int. J. Remote Sens. 38, 1737–1757. doi:10.1080/01431161.2017.1285503

Frappart, F., Calmant, S., Cauhopé, M., Seyler, F., Cazenave, A., 2006a. Preliminary results of ENVISAT RA-2-derived water levels validation over the Amazon basin. Remote Sens. Environ. 100, 252–264. doi:10.1016/j.rse.2005.10.027

Frappart, F., Fatras, C., Mougin, E., Marieu, V., Diepkilé, A.T., Blarel, F., Borderies, P., 2015a. Radar altimetry backscattering signatures at Ka, Ku, C, and S bands over West Africa. Phys. Chem. Earth Parts ABC 83–84, 96–110. doi:10.1016/j.pce.2015.05.001

Frappart, F., Legrésy, B., Niño, F., Blarel, F., Fuller, N., Fleury, S., Birol, F., Calmant, S., 2016. An ERS-2 altimetry reprocessing compatible with ENVISAT for long-term land and ice sheets studies. Remote Sens. Environ. 184, 558–581. doi:10.1016/j.rse.2016.07.037

Frappart, F., Minh, K.D., L'Hermitte, J., Cazenave, A., Ramillien, G., Le Toan, T., Mognard-Campbell, N., 2006. Water volume change in the lower Mekong from satellite altimetry and imagery data. Geophys. J. Int. 167, 570–584. doi:10.1111/j.1365-246X.2006.03184.x

Frappart, F., Papa, F., Marieu, V., Malbeteau, Y., Jordy, F., Calmant, S., Durand, F., Bala, S., 2015b. Preliminary Assessment of SARAL/AltiKa Observations over the Ganges-Brahmaputra and Irrawaddy Rivers. Mar. Geod. 38, 568–580. doi:10.1080/01490419.2014.990591

Frappart, F., Roussel, N., Biancale, R., Martinez Benjamin, J.J., Mercier, F., Perosanz, F., Garate Pasquin, J., Martin Davila, J., Perez Gomez, B., Gracia Gomez, C., Lopez Bravo, R., Tapia Gomez, A., Gili Ripoll, J., Hernandez Pajares, M., Salazar Lino, M., Bonnefond, P., Valles Casanova, I., 2015c. The 2013 Ibiza Calibration Campaign of Jason-2 and SARAL Altimeters. Mar. Geod. 38, 219–232. doi:10.1080/01490419.2015.1008711

Hortle, K.G., 2007. Consumption and the Yield of Fish and Other Aquatic Animals from the Lower Mekong Basin. MRC Technical Paper No16, Mekong River Commission,

670   Vientiane. 87 pp. ISSN: 1383-1489.

671   Huete, A., 1997. A comparison of vegetation indices over a global set of TM images for EOS-
672   MODIS. Remote Sens. Environ. 59, 440–451. doi:10.1016/S0034-4257(96)00112-5

673   Huffman, G.J., Adler, R.F., Bolvin, D.T., Nelkin, E.J., 2010. The TRMM Multi-Satellite
674   Precipitation Analysis (TMPA), in: Gebremichael, M., Hossain, F. (Eds.), Satellite Rainfall
675   Applications for Surface Hydrology. Springer Netherlands, Dordrecht, pp. 3–22.
676   doi:10.1007/978-90-481-2915-7_1

677   Junk, W.J., Brown, M., Campbell, I.C., Finlayson, M., Gopal, B., Ramberg, L., Warner, B.G.,
678   2006. The comparative biodiversity of seven globally important wetlands: a synthesis.
679   Aquat. Sci. 68, 400–414. doi:10.1007/s00027-006-0856-z

680   Kamoshita, A., Ouk, M., 2015. Field level damage of deepwater rice by the 2011 Southeast
681   Asian Flood in a flood plain of Tonle Sap Lake, Northwest Cambodia. Paddy Water
682   Environ. 13, 455–463. doi:10.1007/s10333-014-0463-x

683   Kim, J.-W., Yeh, S.-W., Chang, E.-C., 2014. Combined effect of El Ni?o-Southern
684   Oscillation and Pacific Decadal Oscillation on the East Asian winter monsoon. Clim. Dyn.
685   42, 957–971. doi:10.1007/s00382-013-1730-z

686   Kummu, M., Sarkkula, J., 2008. Impact of the Mekong River Flow Alteration on the Tonle
687   Sap Flood Pulse. AMBIO J. Hum. Environ. 37, 185–192. doi:10.1579/0044-
688   7447(2008)37[185:IOTMRF]2.0.CO;2

689   Kummu, M., Sarkkula, J., Koponen, J., Nikula, J., 2006. Ecosystem Management of the Tonle
690   Sap Lake: An Integrated Modelling Approach. Int. J. Water Resour. Dev. 22, 497–519.
691   doi:10.1080/07900620500482915

692   Lamb, P.J., 1982. Persistence of Subsaharan drought. Nature 299, 46–48. doi:10.1038/299046a0

693   Lamberts, D., 2006. The Tonle Sap Lake as a Productive Ecosystem. Int. J. Water Resour.
694   Dev. 22, 481–495. doi:10.1080/07900620500482592

695   Lemoalle, J., Bader, J.-C., Leblanc, M., Sedick, A., 2012. Recent changes in Lake Chad:
696   Observations, simulations and management options (1973–2011). Glob. Planet. Change
697   80–81, 247–254. doi:10.1016/j.gloplacha.2011.07.004

698   Lim, P., Lek, S., Touch, S.T., Mao, S.-O., Chhouk, B., 1999. Diversity and spatial distribution
699   of freshwater fish in Great Lake and Tonle Sap river (Cambodia, Southeast Asia). Aquat.
700   Living Resour. 12, 379–386. doi:10.1016/S0990-7440(99)00107-2

701   Liu, B., Zhu, C., Su, J., Hua, L., Duan, Y., 2017. Why was the western Pacific subtropical
702   anticyclone weaker in late summer after the 2015/2016 super El Niño?: WEAKENED
703   WPSA FOLLOWING THE 2015/2016 SUPER EL NIñO. Int. J. Climatol.
704   doi:10.1002/joc.5160

705   Lu, X.X., Li, S., Kummu, M., Padawangi, R., Wang, J.J., 2014. Observed changes in the
706   water flow at Chiang Saen in the lower Mekong: Impacts of Chinese dams? Quat. Int. 336,
707   145–157. doi:10.1016/j.quaint.2014.02.006

708   Magnuson, J.J., 2000. Historical Trends in Lake and River Ice Cover in the Northern
709   Hemisphere. Science 289, 1743–1746. doi:10.1126/science.289.5485.1743

710   Mantua, N.J., Hare, S.R., Zhang, Y., Wallace, J.M., Francis, R.C., 1997. A Pacific
711   Interdecadal Climate Oscillation with Impacts on Salmon Production. Bull. Am. Meteorol.
712   Soc. 78, 1069–1079. doi:10.1175/1520-0477(1997)078<1069:APICOW>2.0.CO;2

713   MRC, 1999. Hydrographic Atlas of 1999 for the Tonle Sap River and the Tonle Sap Lake.
714   Mekong River Commission (MRC), Phnom Penh, Cambodia.

715   MRC, 2003. State of the Basin Report: 2003. Mekong River Commission, Phnom Penh,
716   Cambodia. 316 pp. ISSN: 1728–3248.

717   MRC, 2005. Overview of the Hydrology of the Mekong Basin. Mekong River Commission,
718   Vientiane, November 2005; 82.

719   MRCS/WUP-FIN, 2006. Technical Paper No. 5 - Tonle Sap Lake Water Balance
720   Calculations, WUP-FIN Phase II - Hydrological, Environmental and Socio-Economic

Modeling Tools for the Lower Mekong Basin Impact Assessment. Mekong River Commission and Finnish Environment Institute Consultancy Consortium, Vientiane, Lao PDR, 32 pp.

Newman, M., Compo, G.P., Alexander, M.A., 2003. ENSO-Forced Variability of the Pacific Decadal Oscillation. J. Clim. 16, 3853–3857. doi:10.1175/1520-0442(2003)016<3853:EVOTPD>2.0.CO;2

Normandin, C., Frappart, F., Lubac, B., Bélanger, S., Marieu, V., Blarel, F., Robinet, A., and Guiastrennec-Faugas, L., 2018. Quantification of surface water volume changes in the Mackenzie Delta using satellite multi-mission data. Hydrol. Earth Syst. Sci, 22, 1543-1561, doi: 10.5194/hess-22-1543-2018.

Rainboth, W.J., 1996. Fishes of the Cambodian Mekong. FAO Species Identification Field Guide for Fishery Purposes. FAO, Rome, ISBN 92-5-103743-4.

Räsänen, T.A., Kummu, M., 2013. Spatiotemporal influences of ENSO on precipitation and flood pulse in the Mekong River Basin. J. Hydrol. 476, 154–168. doi:10.1016/j.jhydrol.2012.10.028

Rayner, N.A., 2003. Global analyses of sea surface temperature, sea ice, and night marine air temperature since the late nineteenth century. J. Geophys. Res. 108. doi:10.1029/2002JD002670

Rosenzweig, C., Casassa, G., Karoly, D.J., Imeson, A., Liu, C., Menzel, A., Rawlins, S., Root, T.L., Seguin, B., Tryjanowski, P., 2007. Assessment of observed changes and responses in natural and managed systems. Climate Change 2007: Impacts, Adaptation and Vulnerability. Contribution of Working Group II to the Fourth Assessment Report of the Intergovernmental Panel on Climate Change, Parry, M.L., Canziani, O.F., Palutikof, J.P., van der Linden, P.J., Hanson, C.E., Eds., Cambridge University Press, Cambridge, UK, 79-131.

Sakamoto, T., Van Nguyen, N., Kotera, A., Ohno, H., Ishitsuka, N., Yokozawa, M., 2007. Detecting temporal changes in the extent of annual flooding within the Cambodia and the Vietnamese Mekong Delta from MODIS time-series imagery. Remote Sens. Environ. 109, 295–313. doi:10.1016/j.rse.2007.01.011Santos da Silva, J., Calmant, S., Seyler, F., Rotunno Filho, O.C., Cochonneau, G., Mansur, W.J., 2010. Water levels in the Amazon basin derived from the ERS 2 and ENVISAT radar altimetry missions. Remote Sens. Environ. 114, 2160–2181. doi:10.1016/j.rse.2010.04.020

Schindler, D.W., 2009. Lakes as sentinels and integrators for the effects of climate change on watersheds, airsheds, and landscapes. Limnol. Oceanogr. 54, 2349–2358. doi:10.4319/lo.2009.54.6_part_2.2349

Siev, S., Paringit, E., Yoshimura, C., Hul, S., 2016. Seasonal Changes in the Inundation Area and Water Volume of the Tonle Sap River and Its Floodplain. Hydrology 3, 33. doi:10.3390/hydrology3040033

Stone, R., 2010. Severe Drought Puts Spotlight on Chinese Dams. Science 327, 1311–1311. doi:10.1126/science.327.5971.1311

Sverdrup-Jensen, S., 2002. Fisheries in the Lower Mekong Basin: Status and Perspectives. MRC Technical Paper No6, Mekong River Commission, Phnom Penh. 130 pp. ISSN: 1683-1489.

Tangdamrongsub, N., Ditmar, P.G., Steele-Dunne, S.C., Gunter, B.C., Sutanudjaja, E.H., 2016. Assessing total water storage and identifying flood events over Tonlé Sap basin in Cambodia using GRACE and MODIS satellite observations combined with hydrological models. Remote Sens. Environ. 181, 162–173. doi:10.1016/j.rse.2016.03.030

UNESCO (2006). Biosphere Reserves - World network, UNESCO - MAB Secretariat, Paris, France. Available at: http://www.unesco.org/mab/.

Västilä, K., Kummu, M., Sangmanee, C., Chinvanno, S., 2010. Modelling climate change impacts on the flood pulse in the Lower Mekong floodplains. J. Water Clim. Change 01,

67. doi:10.2166/wcc.2010.008

Vu, P-L., Frappart, F., Darrozes, J., Marieu, V., Blarel, F., Ramillien, G., Bonnefond, P., Birol, F., 2018. Multi-Satellite Altimeter Validation along the French Atlantic Coast in the Southern Bay of Biscay from ERS-2 to SARAL. Remote Sensing 10(1), 93. doi:10.3390/rs10010093

Wang, B., Fan, Z., 1999. Choice of South Asian Summer Monsoon Indices. Bull. Am. Meteorol. Soc. 80, 629–638. doi:10.1175/1520-0477(1999)080<0629:COSASM>2.0.CO;2

Wang, B., Wu, R., Lau, K.-M., 2001. Interannual Variability of the Asian Summer Monsoon: Contrasts between the Indian and the Western North Pacific–East Asian Monsoons*. J. Clim. 14, 4073–4090. doi:10.1175/1520-0442(2001)014<4073:IVOTAS>2.0.CO;2

Williamson, C.E., Saros, J.E., Schindler, D.W., 2009. CLIMATE CHANGE: Sentinels of Change. Science 323, 887–888. doi:10.1126/science.1169443

Williamson, C.E., Saros, J.E., Vincent, W.F., Smol, J.P., 2009. Lakes and reservoirs as sentinels, integrators, and regulators of climate change. Limnol. Oceanogr. 54, 2273–2282. doi:10.4319/lo.2009.54.6_part_2.2273

WUP-FIN (2003) Modelling Tonle Sap for Environmental Impact Assessment and Management Support, MRCS/WUP-FIN Project. Final Report (Phnom Penh: Mekong River Commission).

Figures:

Figure 1: a) The Tonle Sap watershed (cyan) is located in the Mekong River Basin (black), the Mekong River and its major tributaries appear in blue; b) 10-day (Jason-1, 2 and 3 in red) and 35-day (ERS-2, ENVISAT and SARAL in green) repeat period tracks over the Tonle Sap Lake watershed. Mekong River Basin boundary and drainage networkcome from the Major River Basins of the World from the Global Runoff Data Centre - Federal Institute of Hydrology (BfG) available at http://www.bafg.de/GRDC/EN/02_srvcs/22_gslrs/221_MRB/riverbasins_node.html. Tonle Sap boundaries were provided by Open Development Cambodia (http://www.opendevelopmentcambodia.net/maps/downloads/). Altimetry tracks were provided by AVISO+ (https://www.aviso.altimetry.fr/en/data/tools/pass-locator.html). Background images come from Google Earth.
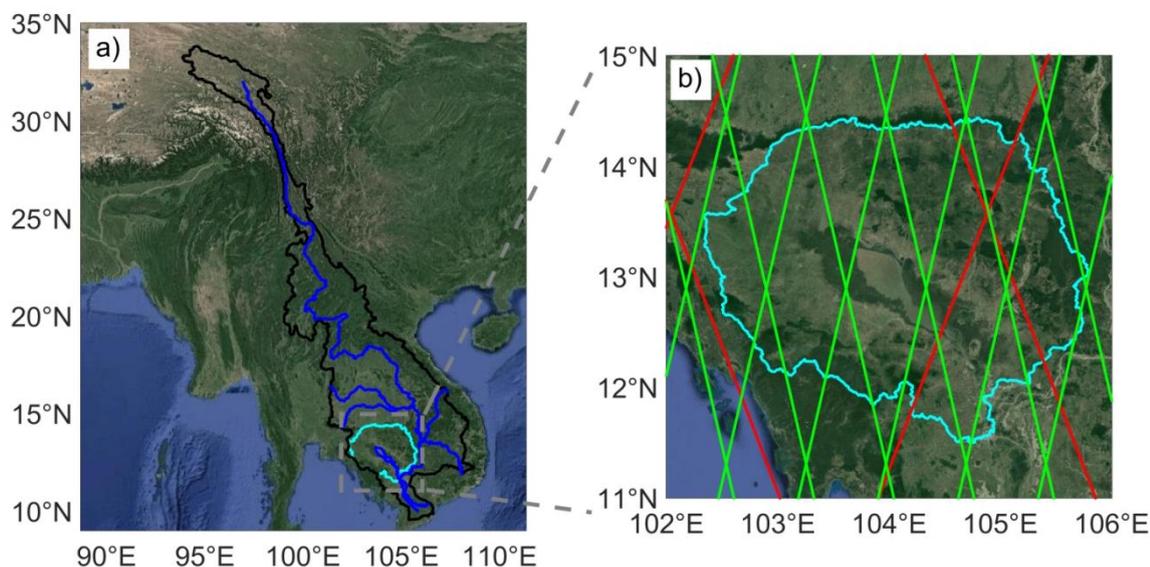
Figure 2: a) Maps of annual flood duration averaged over 2000/2017 time period and b) associated standard deviations expressed in days, using only pixels classified as "inundated". c) Maps of flood duration in 2011 (year with the maximum flood extent over the whole time period) and d) in 2015 (year with the minimum flood extent), considering only pixels classified as inundated. Background images come from Google Earth.
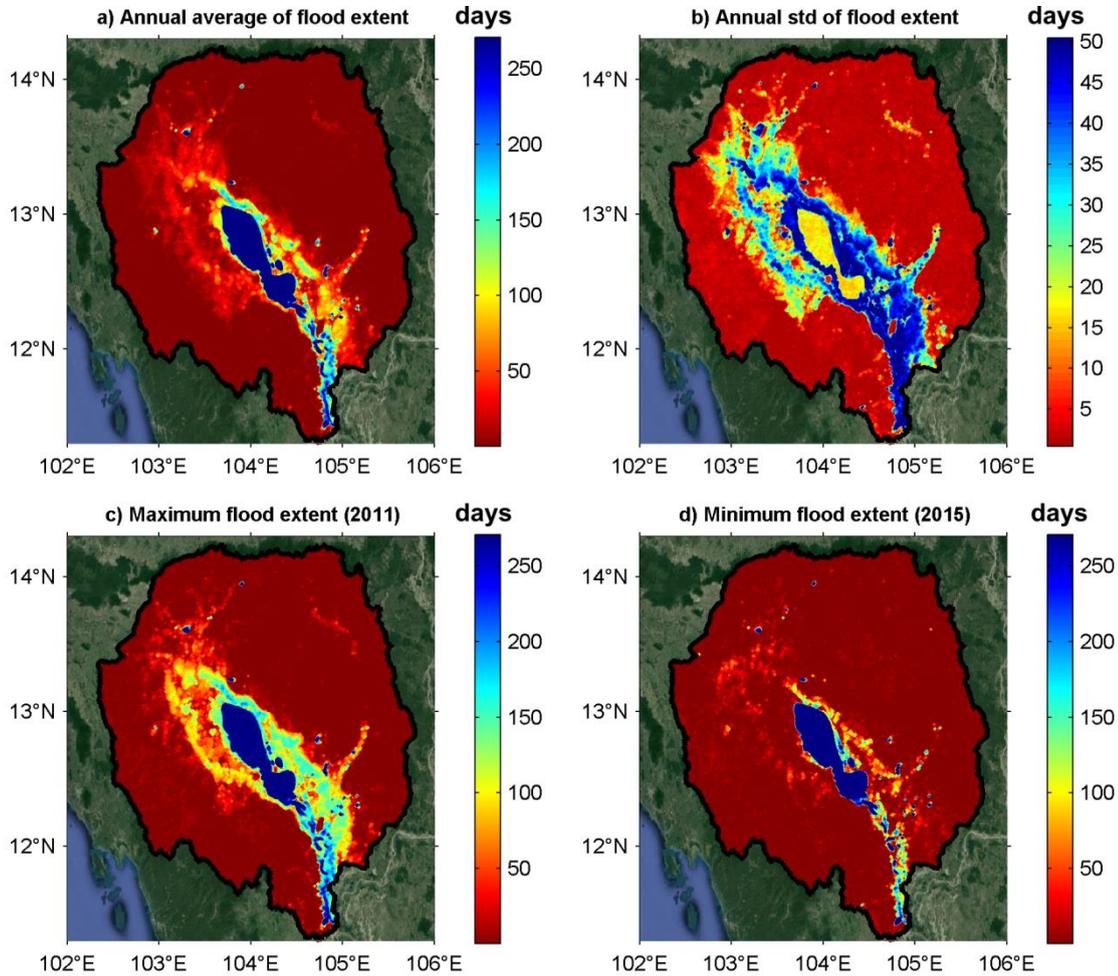
Figure 3: a) Maps of annual flood duration averaged over 2000/2017 time period and b) associated standard deviations expressed in days, using pixels classified as "inundated" and pixels classified as "mixed pixels". c) Maps of flood duration in 2011 (year with the maximum flood extent) and d) in 2015 (year with the minimum flood extent), considering inundated and mixed pixels. Background images come from Google Earth.
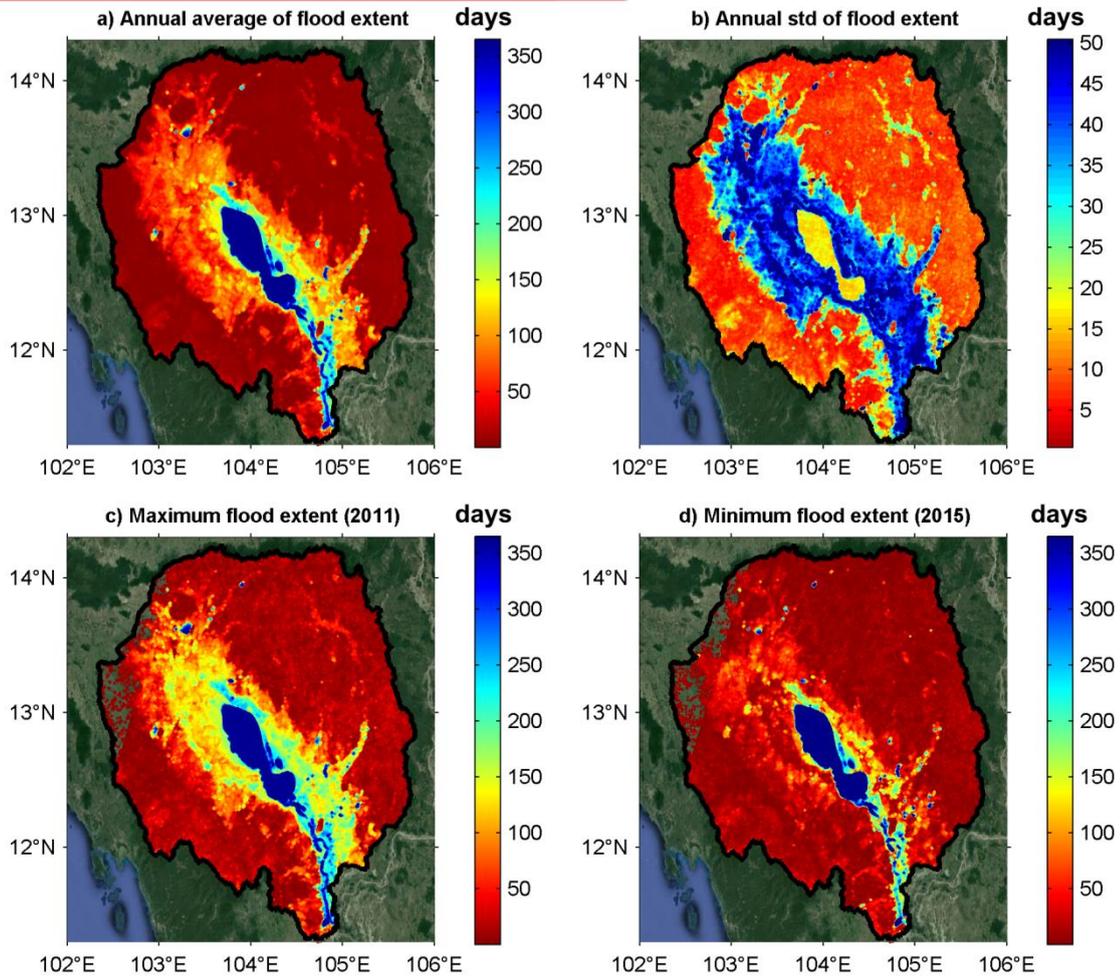
Figure 4: Time series of a) surface water extent (in km^2) in the Tonle Sap basin based on the processing of MODIS images, over 2000-2017, b) altimetry-based water level of the Tonle Sap Lake (in m wrt EGM08 geoid), combining information from Topex/Poseidon (1993-2002), ERS-2 (1995-2003), Jason-1 (2002-2008), ENVISAT (2003-2010), Jason-2 (2008-2016), SARAL (2013-2016) and Jason-3 (since 2016), c) water volume variations of the Tonle Sap lake obtained applying the surface-height relationship over 1993-2017.
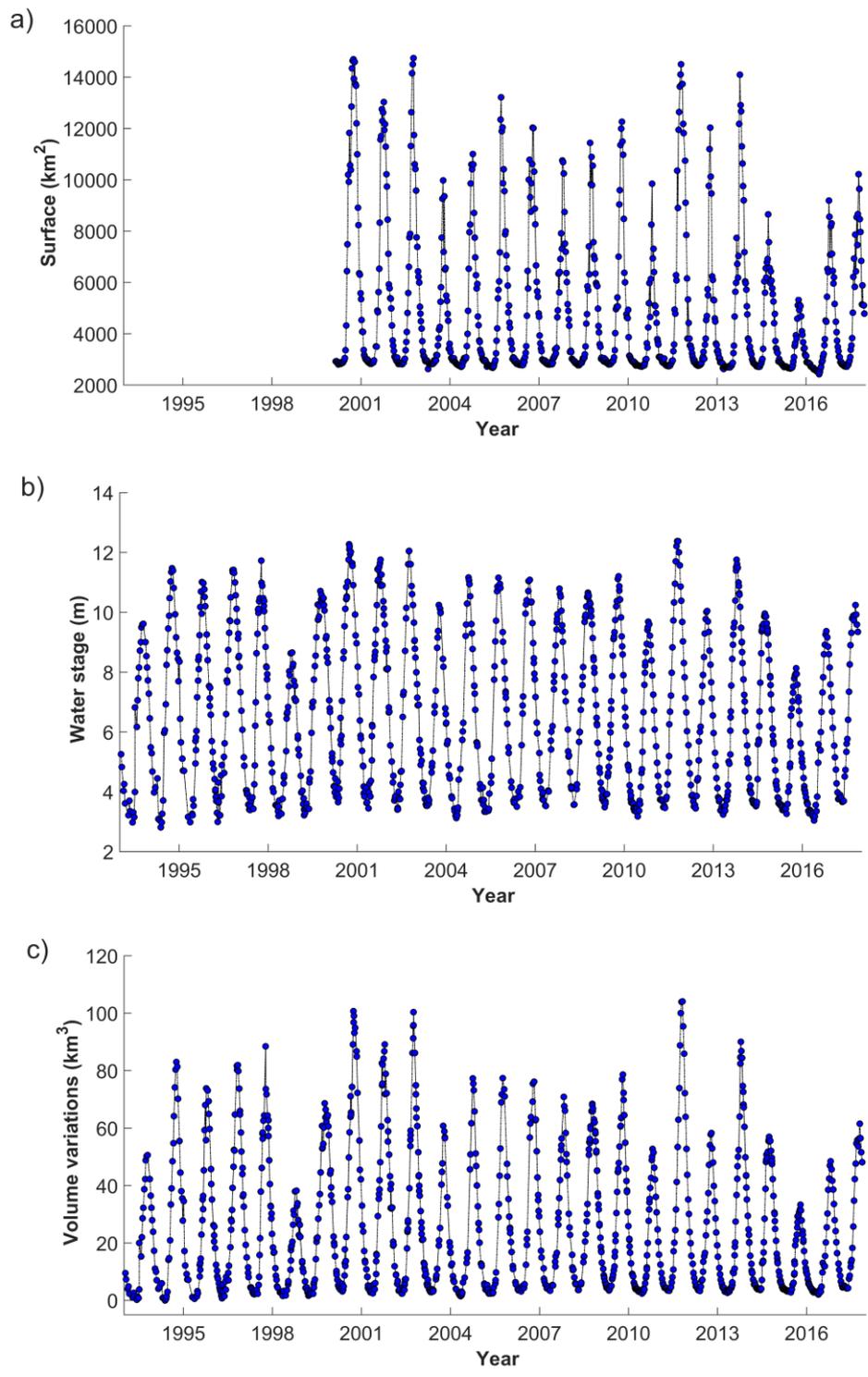
822   Figure 5: a) Interannual variations of annual surface water storage. b) Annual, c) dry and d) wet
823   seasons SPAI in the Mekong Basin and in the Tonle Sap watershed.

824
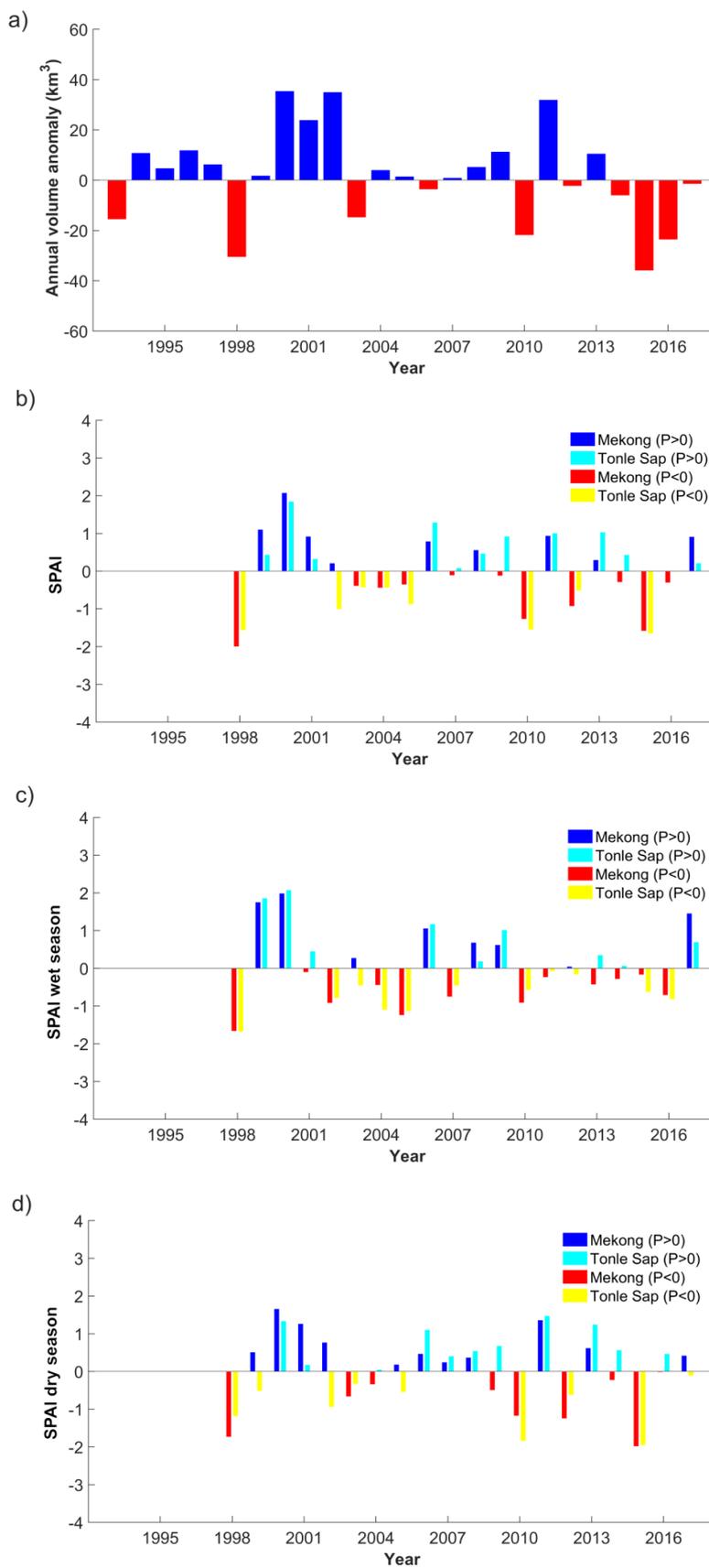
Figure 6: Interannual variations of monthly a) surface water volume of the Tonle Sap watershed, b)
anomalies of ENSO 3.4 and c) PDO indices over 1993-2017.
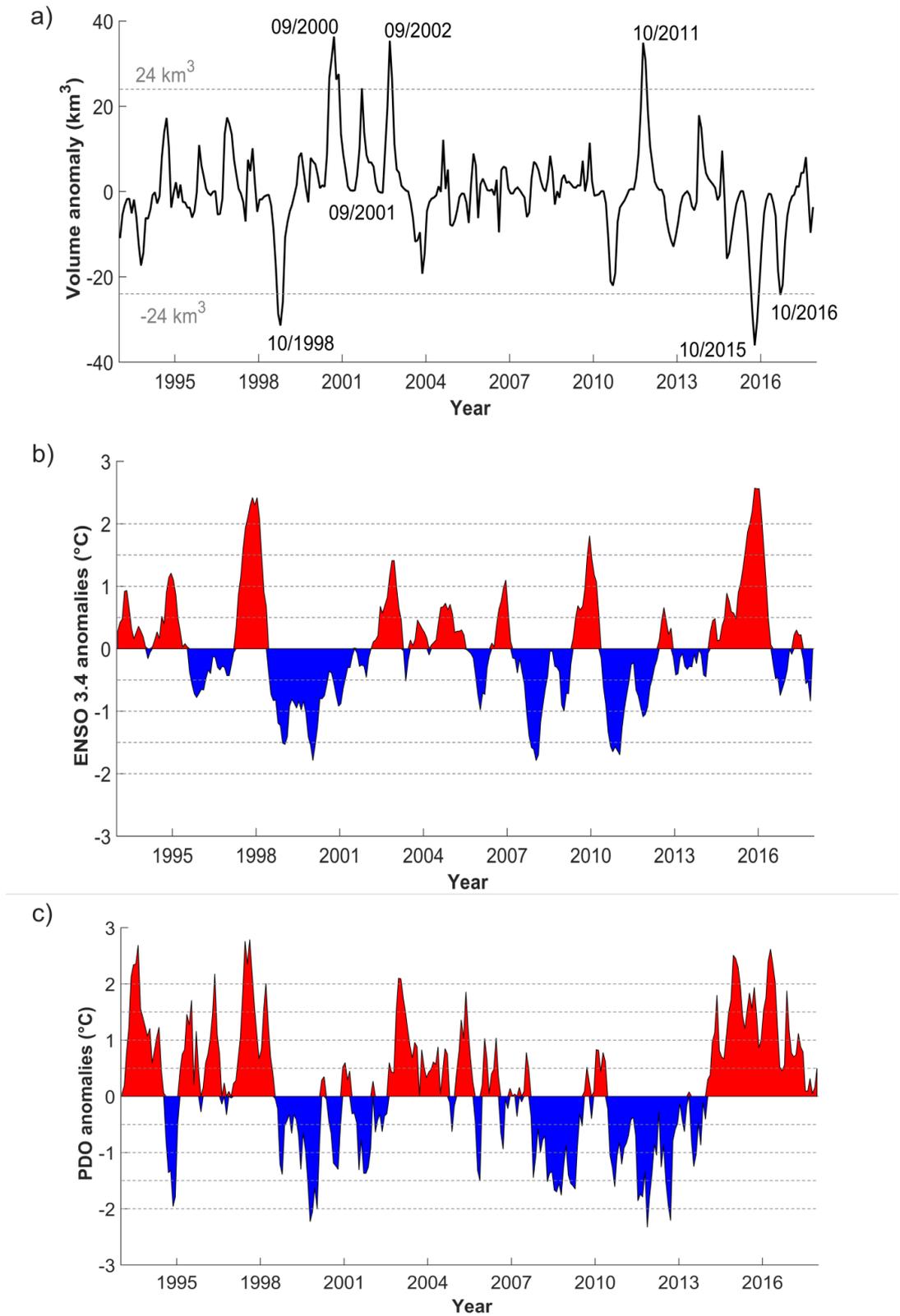
Figure 7: Interannual variations of annual a) surface water storage between 1993 and 2017, b) anomalies of ENSO 3.4 averaged over December to February (DJF) and c) PDO averaged over November to March (NDJF).
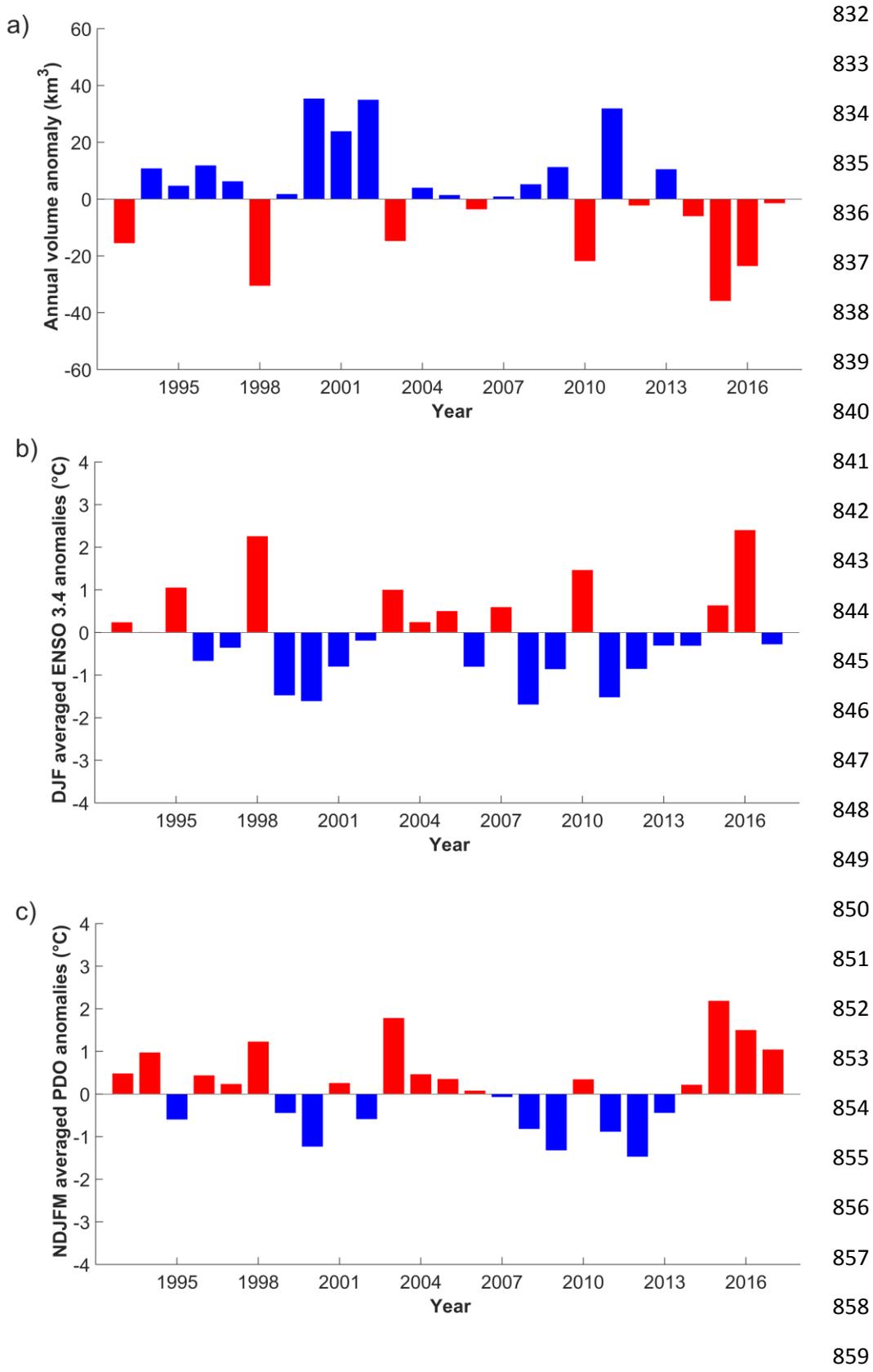
Figure 8: a) Land cover map of the Tonle Sap watershed from the 500 m MODIS-based Global Land Cover Climatology, b) time series of EVI and c) EVI interannual anomaly averaged over Evergreen Broadleaf Forest (green), Woody Savannas (orange) and Cropland/Natural Vegetation Mosaic (black).
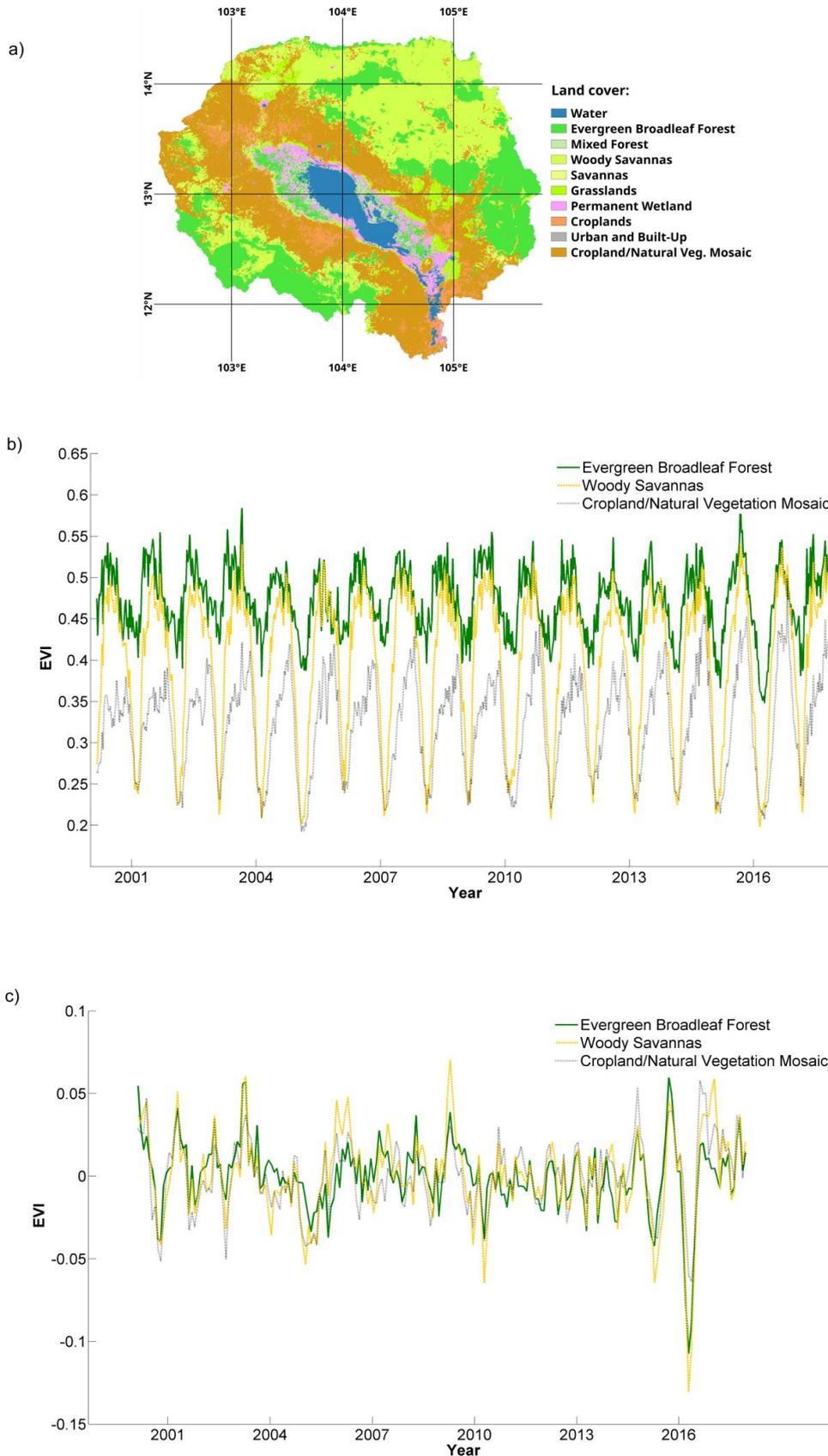
864

865   Figure 9: Anomaly maps of EVI over the Tonle Sap watershed for a) April and b) May (b) 2016.

866
867
868
869
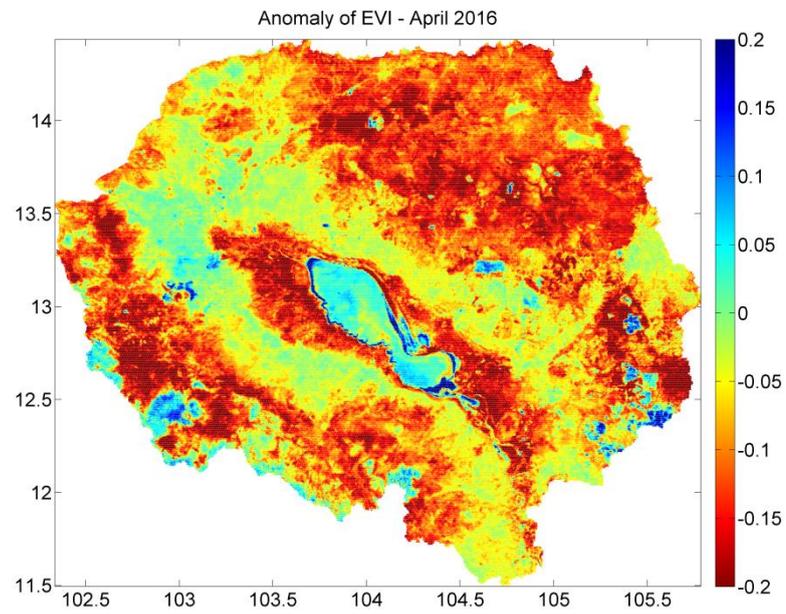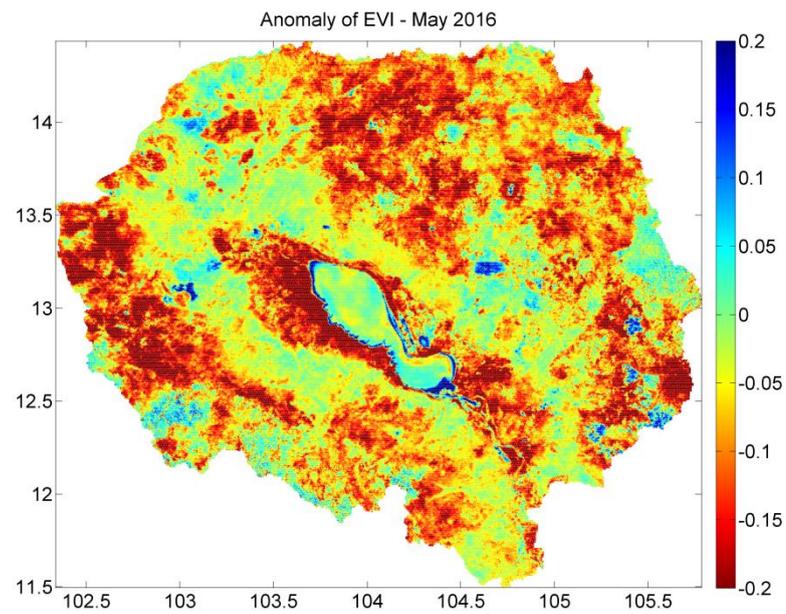
Figure 10: Monthly variations of EVI averaged over 2000-2017 (continuous line) and EVI for 2016
(dotted line) for the Evergreen Broadleaf Forest (green), Woody Savannas (orange) and
Cropland/Natural Vegetation Mosaic (black).